



Cite this: *Nanoscale*, 2017, **9**, 17074

Dipole-induced exchange bias†

Felipe Torres,^{a,b} Rafael Morales,^{ib} c,d Ivan K. Schuller^e and Miguel Kiwi^{ib} a,b

Received 26th July 2017,
Accepted 2nd October 2017

DOI: 10.1039/c7nr05491b

rsc.li/nanoscale

The discovery of dipole-induced exchange bias (EB), switching from negative to positive sign, is reported in systems where the antiferromagnet and the ferromagnet are separated by a paramagnetic spacer (AFM–PM–FM). The magnitude and sign of the EB is determined by the cooling field strength and the PM thickness. The same cooling field yields negative EB for thin spacers, and positive EB for thicker ones. The EB decay profile as a function of the spacer thickness, and the change of sign, are attributed to long-ranged dipole coupling. Our model, which accounts quantitatively for the experimental results, ignores the short range interfacial exchange interactions of the usual EB theories. Instead, it retains solely the long range dipole field that allows for the coupling of the FM and AFM across the PM spacer. The experiments allow for novel switching capabilities of long range EB systems, while the theory allows description of the structures where the FM and AFM are not in atomic contact. The results provide a new approach to design novel interacting heterostructures.

1. Introduction

Exchange Bias (EB)^{1,2} is a phenomenon that has attracted much attention because of its basic scientific interest and relevant technological applications such as spin valves,^{1,3} magnetic sensors,⁴ and spintronic devices.^{5,6} EB was discovered by Meiklejohn and Bean⁷ in Co clusters embedded in CoO, and its fingerprint is the off-center shift of the hysteresis cycle, due to the coupling between a FM and an AFM. For low cooling fields the hysteresis loop shift is negative (NEB), *i.e.* opposite to the applied field;^{1,8} in contrast, for large cooling fields the shift can be positive (PEB).^{9–11} On the basis of experimental results several models have been developed which explain many aspects of EB.^{1,8,12,13} However, additional features have been discovered: the coexistence of NEB and PEB in FM–AFM bilayers, due to hysteresis sub loops that shift in opposite directions,¹⁴ and negative long range exchange bias coupling through a paramagnetic spacer in FM–PM–AFM trilayers.^{15–20} These interesting effects, with potential technological applications such as tunable EB-based devices,¹⁴ constitute a step

forward in the field of EB. Moreover, it has been recently demonstrated that long-range interactions play a key role in stabilizing isolated skyrmions²¹ and in controlling localized spin structures at the nanoscale.²² Thus, a full understanding of the physical mechanism of long-range interactions is essential for designing layered structures with novel spin textures.

2. Results and model

We report the observation of long range switching, from negative to positive EB in FeF₂/Au/Ni trilayers, and provide a theoretical model that describes the results. PEB and NEB can be tuned as a function of both the field cooling strength H_{FC} , and the PM thickness. In order to investigate this long-range FM–AFM coupling an FeF₂ (70 nm)/Au(t_{PM})/Ni (30 nm)/Al (2 nm) wedge-shaped trilayer was fabricated by electron beam evaporation, at a base pressure of 5×10^{-7} Torr. FeF₂ was deposited onto an MgF₂ (110) single crystal at 300 °C. The temperature was reduced to 150 °C for the deposition of Au, Ni and the Al protecting layer. A shadow blade covered progressively the sample during Au growth, in order to obtain the wedge-shaped Au layer, which varies in thickness from $t_{PM} = 0$ to 13 nm. As a consequence a PM wedge with a slope of 0.5 nm mm^{-1} is obtained. The magneto-optical Kerr effect (MOKE, with a 100 μm diameter laser spot was used to measure local hysteresis loops as a function of Au thickness.

2.1. Experimental results

FeF₂ grows epitaxially on MgF₂ following the same (110) orientation. This crystallographic plane exhibits a magnetically

^aDepto. de Física, Facultad de Ciencias, Universidad de Chile, Casilla 653, Santiago, Chile 7800024

^bCentro para el Desarrollo de la Nanociencia y la Nanotecnología, CEDENNA, Avda. Ecuador 3493, Santiago, Chile 9170124. E-mail: m.kiwi.t@gmail.com

^cDepartment of Chemical-Physics & BCMaterials, University of the Basque Country UPV/EHU, 48940 Leioa, Spain

^dIKERBASQUE, Basque Foundation for Science, 48011 Bilbao, Spain

^eDepartment of Physics and Center for Advanced Nanoscience, University of California San Diego, La Jolla, California 92093, USA

†Electronic supplementary information (ESI) available. See DOI: 10.1039/c7nr05491b

compensated spin structure in a bulk single crystal. MOKE hysteresis loops were measured at 50 K, below the FeF_2 Néel temperature (78 K) after field cooling under H_{FC} , as shown in Fig. 1(a–c). The MOKE hysteresis loops were obtained by probing several positions on the sample. Three cooling fields were selected to illustrate different cases: (i) weak cooling fields ($H_{\text{FC}} = 100$ Oe) yield negative exchange bias (NEB) for all spacer thicknesses, as seen in Fig. 1(a). (ii) For intermediate cooling fields ($H_{\text{FC}} = 500$ Oe) the H_{EB} dependence with t_{PM} displays both regimes: NEB for thin Au layers, and PEB for thicker spacer layers, as shown in Fig. 1(b). (iii) Large cooling

fields ($H_{\text{FC}} = 2500$ Oe) lead to hysteresis loops with only positive exchange bias (PEB), as shown in Fig. 1(c).

As shown in Fig. 1(b), two H_{EB} values of opposite sign coexist for the same t_{Au} . The NEB/PEB ratio evolves with t_{Au} , with an increasing (decreasing) contribution of PEB (NEB) sub-loops as t_{Au} increases. This coexistence is attributed to the local distribution of long-range coupling strengths in the area probed by the laser spot, as explained below.

2.2. Theoretical model

In order to explain the above experimental results we put forward a model whose main features are: (i) the breaking of the AFM magnetic symmetry in the vicinity of the AFM–PM interface due to the coupling between uncompensated magnetic moments in the AFM and the FM,^{23–25} the interaction with the external magnetic field^{12,26} and the inherent magnetic defects at the AFM–PM interface,^{1,2,8} which break the balance between the magnetic moment averages of the sublattices; (ii) a long range dipolar coupling between the magnetic domains in the FM and the AFM. While the influence of the AFM domain size on EB in AFM/FM bilayers has been extensively examined,^{27–29} a deep understanding of long range coupling across a spacer is still not available; and (iii) the competition of the strength of the applied and dipolar fields that controls the magnitude and sign of the exchange bias, by varying the size of the magnetic domains induced at the FM–PM. We assume that the domains in the AFM, which are due to the energy balance and that originate EB, are created during field cooling and remain frozen even when the FM is fully saturated, as observed experimentally in exchange coupled bilayers.^{24,30–33} As shown in Fig. 2(a), during the field cooling process FM layers are fully saturated and magnetic domains are nucleated at AFM, simultaneously. At zero field cooling as seen in Fig. 2(b), FM domains are formed due to a remanent dipole field. This differs from the conventional approach that attributes EB to interface exchange, between two differently ordered magnetic materials in close atomic contact, and whose main ingredient is the exchange coupling between the FM and the AFM. Moreover, no FM–PM or AFM–PM exchange interactions are included here. Therefore, H_{EB} does depend on the spacer thickness, and consequently the presence of a spacer is a *sine qua non* requirement for our model, but it restricts our results to PM thicknesses larger than 5 Å, since when $t_{\text{PM}} \leq 5$ Å the exchange coupling between the AFM and the FM cannot be ignored.

Our assumption about AFM domains is based on photo-emission, electron microscopy and X-ray magnetic circular dichroism measurements,^{30,34} by the formation of a two domain state, composed of uncompensated spins, as observed experimentally.^{14,35,36} Since for large cooling fields the anisotropy energy is significantly larger than the dipolar and Zeeman energies, these domains remain frozen during the hysteresis cycle. In fact the dipolar coupling, and therefore EB, depends on the long range dipolar coupling between the FM and the AFM, and the formation of the AFM domains. The latter in turn is determined by the symmetry breaking of the

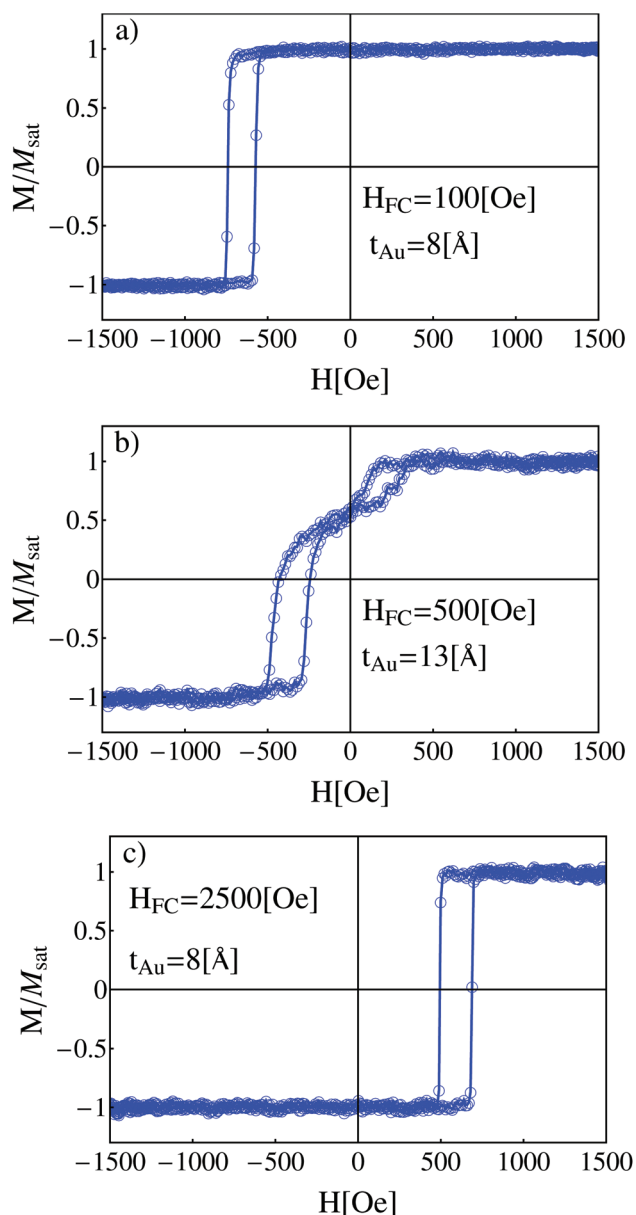


Fig. 1 MOKE hysteresis loops measured at 50 K, after cooling under three different fields. (a) $H_{\text{FC}} = 100$ [Oe] (NEB); (b) $H_{\text{FC}} = 500$ [Oe] (NEB/PEB); and (c) $H_{\text{FC}} = 2500$ [Oe] (PEB). Empty-symbols: experimental data. M_{sat} is the saturated magnetization. Solid lines have been added as guide to the eye.

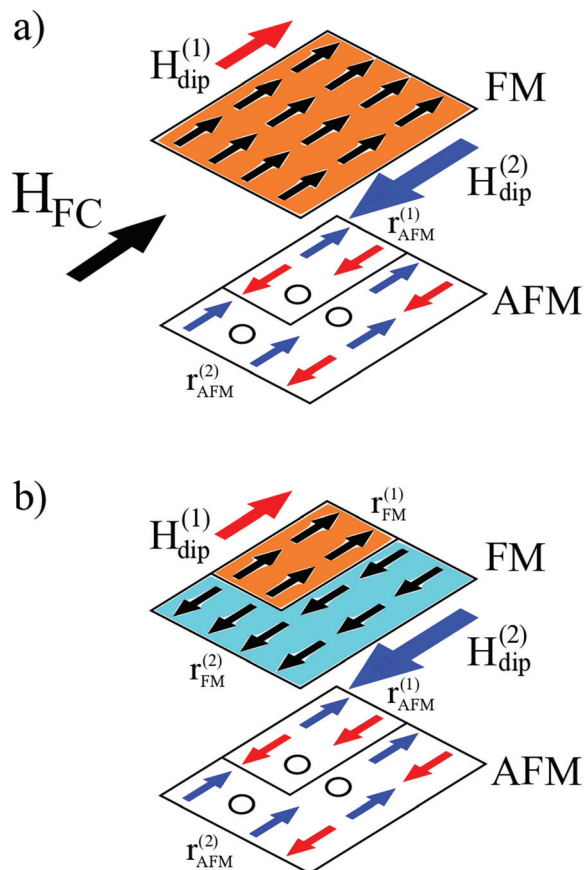


Fig. 2 Illustration of the (a) field cooling and (b) zero field cooling AFM/PM/FM trilayers. For simplicity, the schematic spin configuration at the one FM and one AFM layer is shown. (a) FM layers are fully saturated along the field cooling, while AFM layers break into magnetic domains formed by uncompensated spins. The effective size of the AFM domains oriented opposite and along H_{FC} are $r_{AFM}^{(1)}$ and $r_{AFM}^{(2)}$. The red and blue arrows represent the concomitant dipole fields $H_{dip}^{(1)}$ and $H_{dip}^{(2)}$, respectively. (b) Due to the dipole field, FM domain patterns are induced even under zero field cooling. The effective size of the induced FM domains are $r_{FM}^{(1)}$ and $r_{FM}^{(2)}$.

magnetic sublattices. On this basis our model predicts the magnitude of the average AFM domain magnetization as a function of the spacer width and the H_{FC} strength.

The physics of the microscopic mechanism of the magnetization reversal mode, after field cooling, is illustrated in Fig. 3 (a–c), at $H_{FC} = 100, 500$, and 2500 (Oe); for simplicity, let us consider a small fraction of the $FeF_2/Au/Ni$ trilayer composed of two magnetic oppositely oriented AFM domains, only the FM–PM and AFM–PM are shown in Fig. 3. During field cooling, AFM domains with opposite net magnetizations arise from the competition between the Zeeman energy and the dipolar interaction with the saturated FM. After cooling at zero field, below the Néel temperature, the spin structure on the FM–PM interface is related to the AFM domain pattern, displaying the coexistence of magnetic domains with opposite orientations on the FM. When the field is swept during the hysteresis cycle the magnetic domain formation on the FM is

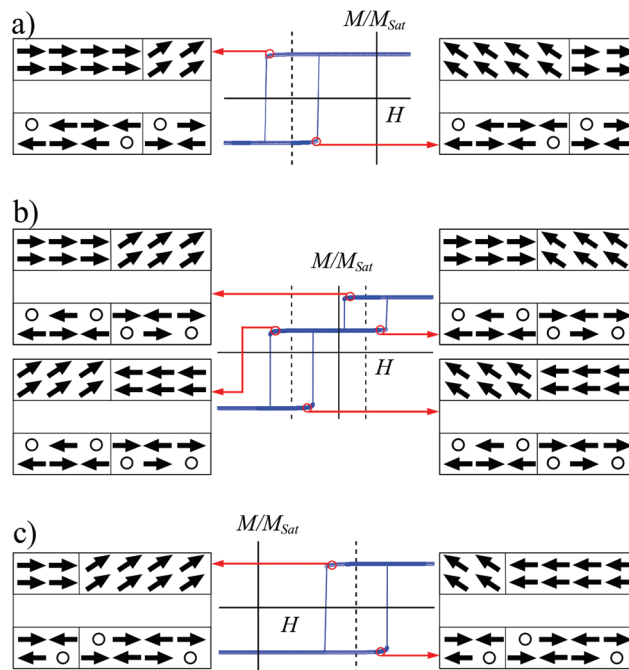


Fig. 3 The hysteresis loops, and a graphical illustration of the spin configuration at the AFM and FM layers during magnetization reversal, after field cooling. For a weak applied field the magnetization state of the FM arises from the competition between the dipole field generated by the AFM domains, and the applied field. The remanent magnetization is a function of the ratio of the sizes of these two kinds of magnetic domains. (a) $H_{FC} = 100$ [Oe] (NEB); (b) $H_{FC} = 500$ [Oe] (NEB/PEB); and (c) $H_{FC} = 2500$ [Oe] (PEB). The black open circles correspond to the randomly distributed magnetic vacancies.

determined by the competition between the formation of large domains induced by the Zeeman interaction and the formation of small domains due to the local dipole fields.³⁰

The FM–AFM interaction energy density of two noninteracting FM domains is given by

$$E_{\text{int}}(\theta_1, \theta_2) = -K_{\text{FM}}[\cos^2(\beta - \theta_1) + \cos^2(\beta - \theta_2)] - M_{\text{FM}}\mu_0[\cos(\theta_1) + \cos(\theta_2)]H + E_{\text{dip}}, \quad (1)$$

where μ_0 is the vacuum permeability, β is the angle between the applied field (H) and the FM anisotropy axis. θ_1 and θ_2 are the angles between the applied field and the magnetization of domains-1 and 2. The first term of eqn (1) is the contribution of the FM uniaxial anisotropy energy (K_{FM}), the second corresponds to the Zeeman energy, and the last one is the energy contribution of the dipole interaction E_{dip} . The FM domain-2 reverts with an additional energy cost to yield PEB. In contrast, the FM domain-1 reverts in the opposite direction and yields NEB, as is seen below. Therefore, the dipolar term in eqn (1) takes the form

$$E_{\text{dip}} = \frac{\mu_0 M_{\text{FM}} m_{\text{AFM}}}{4\pi t_{\text{PM}}^3} \left[\frac{r_{\text{FM}}^{(2)}}{r_{\text{AFM}}^{(2)}} \cos(\theta_2) - \frac{r_{\text{FM}}^{(1)}}{r_{\text{AFM}}^{(1)}} \cos(\theta_1) \right]. \quad (2)$$

The staggered magnetization is $m_{\text{AFM}} = \mu_B \sum_{\mathbf{r}} \langle S_{\alpha}^z(\mathbf{r}) - S_{\beta}^z(\mathbf{r}) \rangle \neq 0$, \mathbf{r} denotes a lattice site, and μ_B is the Bohr magneton (the details are provided in the ESI†). When the cooling field is applied along the easy axis of an AFM, quantum fluctuations of the frustrated spins break the balance between the two magnetic sublattices,^{13,26} and therefore $|\langle S_{\alpha}^z(\mathbf{r}) \rangle| \neq |\langle S_{\beta}^z(\mathbf{r}) \rangle|$, where $|\langle S_{\alpha}^z(\mathbf{r}) \rangle|$, and $|\langle S_{\beta}^z(\mathbf{r}) \rangle|$ are the average magnetic moments of the two AFM sublattices. A dipole field $H_{\text{dip}}^{\text{AFM}} = \mu_0 m_{\text{AFM}} / (4\pi t_{\text{PM}}^3)$, valid for $t_{\text{PM}} > 5 \text{ \AA}$ as explained above is therefore induced, which couples the AFM domains to the FM domains across the PM spacer of thickness t_{PM} . To obtain the magnetization M we solve $\partial E_{\text{int}}(\theta_1, \theta_2) / \partial \theta_1 = 0 = \partial E_{\text{int}}(\theta_1, \theta_2) / \partial \theta_2$. Hence,

$$M = M_{\text{sat}} \left[\frac{r_{\text{FM}}^{(1)}}{r_{\text{AFM}}^{(1)}} \cos(\theta_1) + \frac{r_{\text{FM}}^{(2)}}{r_{\text{AFM}}^{(2)}} \cos(\theta_2) \right], \quad (3)$$

where M_{sat} is the saturation magnetization. Inspired by Gaunt's model³⁷ we obtain (see details in the ESI†)

$$\frac{r_{\text{FM}}^{(1)}}{r_{\text{AFM}}^{(1)}} = \frac{\rho_1}{\left(1 - \mu_0 (H_{\text{FC}} - H_{\text{dip}}^{\text{AFM}}) M_{\text{FM}} / 2K_{\text{FM}}\right)}, \quad (4)$$

$$\frac{r_{\text{FM}}^{(2)}}{r_{\text{AFM}}^{(2)}} = \frac{\rho_2}{\left(1 + \mu_0 (H_{\text{FC}} + H_{\text{dip}}^{\text{AFM}}) M_{\text{FM}} / 2K_{\text{FM}}\right)}, \quad (5)$$

where $\rho_k = \sqrt{k_B T / K_{\text{FM}} t_{\text{FM}} / r_{\text{AFM}}^{(k)}}$ is the ratio between the size of FM domain- k , induced in the absence of external magnetic fields, and the size of the respective AFM domain- k . Replacing eqn (2), (4), and (5) with eqn (1), one obtains

$$E_{\text{int}}(\theta_1, \theta_2) = -K_{\text{FM}} [\cos^2(\beta - \theta_1) + \cos^2(\beta - \theta_2)] - M_{\text{FM}} \mu_0 (H + H_{\text{NEB}}) \cos(\theta_1) - M_{\text{FM}} \mu_0 (H - H_{\text{PEB}}) \cos(\theta_2), \quad (6)$$

where $H_{\text{NEB}} < 0$ and $H_{\text{PEB}} > 0$ are given by

$$H_{\text{NEB}} = -\frac{m_{\text{AFM}}}{4\pi t_{\text{PM}}^3} \frac{2\rho_1 K_{\text{FM}}}{1 - \mu_0 (H_{\text{FC}} - H_{\text{dip}}^{\text{AFM}}) M_{\text{FM}}}, \quad (7)$$

$$H_{\text{PEB}} = \frac{m_{\text{AFM}}}{4\pi t_{\text{PM}}^3} \frac{2\rho_2 K_{\text{FM}}}{1 + \mu_0 (H_{\text{FC}} + H_{\text{dip}}^{\text{AFM}}) M_{\text{FM}}}. \quad (8)$$

To estimate H_{EB} we compute³² $H_{\text{EB}} = H_{\text{PEB}} + H_{\text{NEB}}$ where $H_{\text{PEB}} > 0$ and $H_{\text{NEB}} < 0$. This way the energy cost of the reversal of these additional magnetic fields generates a double hysteresis loop. The parameters adopted in this calculation^{1,8,26} are $K_{\text{AFM}} = 1.4 \times 10^8 \text{ erg cm}^{-3}$, $K_{\text{FM}} = 5 \times 10^4 \text{ erg cm}^{-3}$, and $M_{\text{FM}} = 484 \text{ emu cm}^{-3}$. An increase of H_{FC} produces an increased dipolar field on the FM in the opposite direction to H_{FC} . This in turn increases the fraction of FM domains oriented opposite to H_{FC} . For $H_{\text{FC}} = 100 \text{ [Oe]}$ the size of the FM domains oriented opposite to H_{FC} is increased, hence negative exchange bias (NEB) prevails (see Fig. 3(a)). For intermediate H_{FC} , double hysteresis loops appear as shown in Fig. 3(b). For $H_{\text{FC}} = 2500 \text{ [Oe]}$ the size of the FM domains oriented along H_{FC} is larger than the size of the FM domains oriented opposite to H_{FC} , and consequently PEB is generated as illustrated in Fig. 3(c).

The ratio of the sizes of the FM and AFM domains critically depends on the only adjustable parameters ρ_1 and ρ_2 . If this distribution is too wide then it quenches the magnetic moments induced by the quantum fluctuations, and the effects disappear. From these results, and assuming that the domain configurations induced by the cooling field in the AFM remain frozen,^{8,10} the EB profile can be obtained using eqn (7) and (8). In fact, the magnetization orientation of the FM is determined by the competition between the dipole field generated by the domains in the AFM, and the applied field. As mentioned above Fig. 4(a–c) show the experimental and theoretical results for the $H_{\text{EB}}(t_{\text{PM}})$ profile as a function of Au spacer thickness, which are

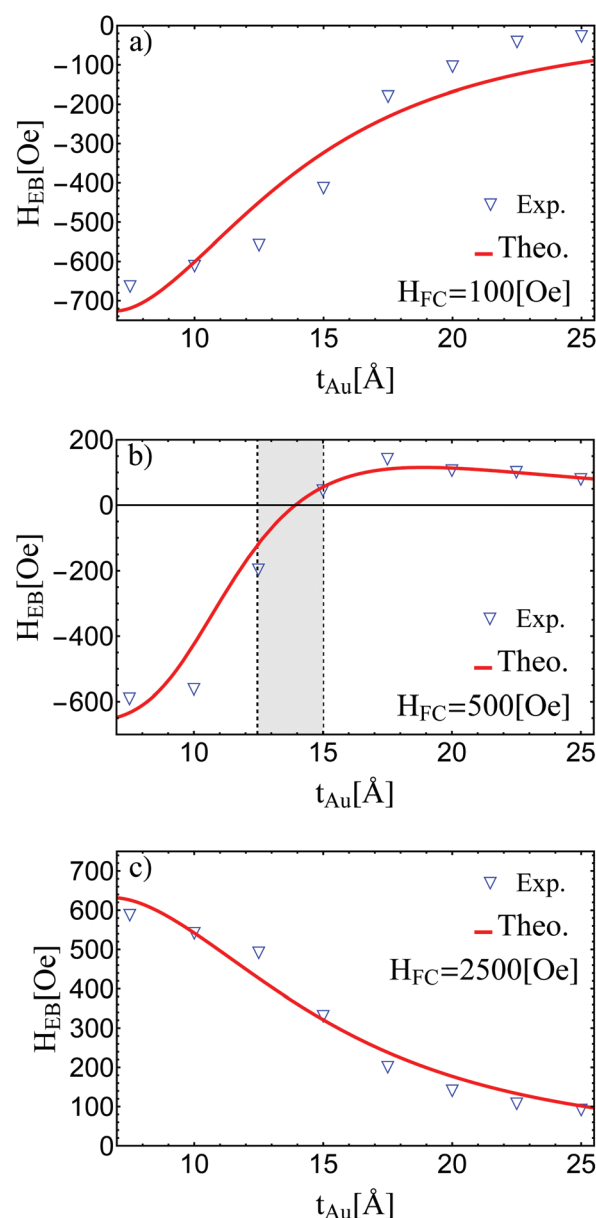


Fig. 4 Au thickness dependence of the exchange bias field after cooling under fields (a) $H_{\text{FC}} = 100 \text{ [Oe]}$ (NEB) ($\rho_1 = 5.3$), (b) $H_{\text{FC}} = 500 \text{ [Oe]}$ (NEB/PEB) ($\rho_1 = 4.5$, and $\rho_2 = 4.3$), and (c) $H_{\text{FC}} = 2500 \text{ [Oe]}$ (PEB) ($\rho_2 = 4.1$). Triangles: experimental data; solid lines: theoretical results.

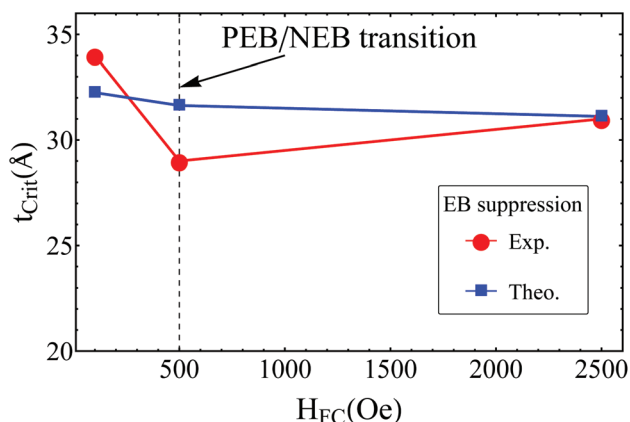


Fig. 5 Critical spacer thickness as a function of cooling field. For all three experimentally determined cooling field strengths no EB is observed beyond $t_{\text{crit}} \approx 30$ Å.

in fairly good agreement with the experimental data (empty-symbols). We found that the fraction of magnetic vacancies required to fit the data is always less than 1%.

In addition, we show in Fig. 5 a plot of the critical thicknesses where the exchange bias vanishes under different cooling fields. For the three experimentally determined cooling field values ($H_{\text{FC}} = 100, 500$ and 2500 Oe) $t_{\text{crit}} \approx 30$ Å. In Fig. 3(b) two sub-loops are observed, in agreement with experiment. The EB profiles for $H_{\text{FC}} = 100$ [Oe] and $H_{\text{FC}} = 2500$ [Oe] are also in agreement with experiment. For $H_{\text{FC}} = 500$ [Oe] and $t_{\text{PM}} = 15$ Å, a transition from NEB to PEB is observed, as shown in Fig. 1(b) and 4(b), which is in good agreement with our theory. It is worth emphasizing that our model yields negative and positive EB, and the NEB/PEB transition, with a single set of parameters.

3. Conclusions

In conclusion, these results show the first evidence for positive and negative EB in AFM/PM/FM trilayers. The sign and magnitude of the H_{EB} can be tuned by the cooling field strength and the paramagnetic spacer thickness. The model, based on magnetic domain formations in the AFM and long range interactions, describes qualitatively and quantitatively the experimental dependence of H_{EB} on the spacer thickness for low and high cooling fields. Moreover, our model accounts for the switching from negative to positive EB observed for a certain PM thickness and intermediate cooling fields. We have shown that the nucleation of oppositely oriented magnetic domain breaks the symmetry and even gives rise to EB when the AFM free original surface is magnetically compensated. This long range interaction could be used to manipulate EB-based devices, such as spin valves and magnetic sensors.

Conflicts of interest

There are no conflicts to declare.

Acknowledgements

This is a highly collaborative research. The experiments were performed jointly, the data were extensively debated and the paper was written by multiple iterations between all the co-authors. Samples were fabricated and characterized at UCSD. Kerr effect measurements were carried out at UPV/EHU. The theoretical calculations were performed at UCh. This research was supported by FONDECYT Projects 1160639 and 1130272 (MK), 1150806 (FT) and CEDENNA (BASAL/CONICYT GRANT FB0807). The UCSD-UCh collaboration was supported by AFOSR Grant FA9550-16-1-0122. The research at UCSD was supported by the Office of Basic Energy Science, U.S. Department of Energy, BES-DMS funded by the Department of Energy, Office of Basic Energy Science, DMR under grant DE FG02 87ER-45332. RM acknowledges support from the European Union FP7 IRSES Grant No. 318901 and Horizon 2020 research and innovation programme under the Marie Skłodowska-Curie grant agreement No 734801, and AEI FIS2013-45469, FIS2016-76058 UE FEDER “Una manera de hacer Europa”.

References

- 1 J. Nogués and I. K. Schuller, *J. Magn. Magn. Mater.*, 1999, **192**, 203–232.
- 2 J. Nogués, J. Sort, V. Langlais, V. Skumryev, S. Suriñach, J. Muñoz and M. Baró, *Phys. Rep.*, 2005, **422**, 65–117.
- 3 B. Dieny, V. S. Speriosu, S. Metin, S. S. P. Parkin, B. A. Gurney, P. Baumgart and D. R. Wilhoit, *J. Appl. Phys.*, 1991, **69**, 4774–4779.
- 4 B. Negulescu, D. Lacour, F. Montaigne, A. Gerken, J. Paul, V. Spetter, J. Marien, C. Duret and M. Hehn, *Appl. Phys. Lett.*, 2009, **95**, 112502.
- 5 T. A. Nguyen, Y. Fang, V. Fallahi, N. Benatmane, S. Mohseni, R. Dumas and J. Åkerman, *Appl. Phys. Lett.*, 2011, **98**, 172502.
- 6 T. Gasi, A. K. Nayak, J. Winterlik, V. Ksenofontov, P. Adler, M. Nicklas and C. Felser, *Appl. Phys. Lett.*, 2013, **102**, 202402.
- 7 W. H. Meiklejohn and C. P. Bean, *Phys. Rev.*, 1956, **102**, 1413.
- 8 M. Kiwi, *J. Magn. Magn. Mater.*, 2001, **234**, 584–595.
- 9 J. Nogués, D. Lederman, T. Moran and I. K. Schuller, *Phys. Rev. Lett.*, 1996, **76**, 4624.
- 10 M. Kiwi, J. Mejía-López, R. Portugal and R. Ramírez, *Solid State Commun.*, 2000, **116**, 315–319.
- 11 M. Kiwi, J. Mejía-López, R. Portugal and R. Ramírez, *EPL*, 1999, **48**, 573.
- 12 G. Mata, E. Pestana, H. Dreyse and M. Kiwi, *Phys. Rev. B*, 2006, **74**, 144407.
- 13 G. Mata, E. Pestana, H. Dreyse and M. Kiwi, *Phys. B*, 2007, **398**, 262–266.

- 14 R. Morales, M. Kovylyna, I. K. Schuller, A. Labarta and X. Batlle, *Appl. Phys. Lett.*, 2014, **104**, 032401.
- 15 N. J. Gökemeijer, T. Ambrose and C. L. Chien, *Phys. Rev. Lett.*, 1997, **79**, 4270.
- 16 L. Thomas, A. J. Kellock and S. S. Parkin, *J. Appl. Phys.*, 2000, **87**, 5061–5063.
- 17 M. Gruyters, M. Gierlings and D. Riegel, *Phys. Rev. B*, 2001, **64**, 132401.
- 18 M.-T. Lin, C. H. Ho, C.-R. Chang and Y. D. Yao, *Phys. Rev. B*, 2001, **63**, 100404.
- 19 J. W. Cai, W. Y. Lai, J. Teng, F. Shen, Z. Zhang and L. M. Mei, *Phys. Rev. B*, 2004, **70**, 214428.
- 20 Y. Meng, J. Li, P.-A. Glans, C. A. Jenkins, E. Arenholz, A. Tan, J. Gibbons, J. S. Park, C. Hwang, H. W. Zhao and Z. Q. Qiu, *Phys. Rev. B*, 2012, **85**, 014425.
- 21 A. Hrabec, J. Sampaio, M. Belmeguenai, I. Gross, R. Weil, S. Chérif, A. Stashkevich, V. Jacques, A. Thiaville and S. Rohart, *Nat. Commun.*, 2017, **8**, 15765.
- 22 F. Hellman, A. Hoffmann, Y. Tserkovnyak, G. S. D. Beach, E. E. Fullerton, C. Leighton, A. H. MacDonald, D. C. Ralph, D. A. Arena, H. A. Dürr, P. Fischer, J. Grollier, J. P. Heremans, T. Jungwirth, A. V. Kimel, B. Koopmans, I. N. Krivorotov, S. J. May, A. K. Petford-Long, J. M. Rondinelli, N. Samarth, I. K. Schuller, A. N. Slavin, M. D. Stiles, O. Tchernyshyov, A. Thiaville and B. L. Zink, *Rev. Mod. Phys.*, 2017, **89**, 025006.
- 23 S. Roy, M. R. Fitzsimmons, S. Park, M. Dorn, O. Petravic, I. V. Roshchin, Z.-P. Li, X. Batlle, R. Morales, A. Misra, X. Zhang, K. Chesnel, J. B. Kortright, S. K. Sinha and I. K. Schuller, *Phys. Rev. Lett.*, 2005, **95**, 047201.
- 24 R. Morales, Z.-P. Li, O. Petravic, X. Batlle, I. K. Schuller, J. Olamit and K. Liu, *Appl. Phys. Lett.*, 2006, **89**, 072504.
- 25 M. R. Fitzsimmons, B. J. Kirby, S. Roy, Z.-P. Li, I. V. Roshchin, S. K. Sinha and I. K. Schuller, *Phys. Rev. B*, 2007, **75**, 214412.
- 26 F. Torres and M. Kiwi, *IEEE Trans. Magn.*, 2014, **50**, 1–4.
- 27 M. R. Fitzsimmons, B. J. Kirby, S. Roy, Z.-P. Li, I. V. Roshchin, S. K. Sinha and I. K. Schuller, *Phys. Rev. B*, 2007, **75**, 214412.
- 28 H. Ohldag, H. Shi, E. Arenholz, J. Stöhr and D. Lederman, *Phys. Rev. Lett.*, 2006, **96**, 027203.
- 29 A. Scholl, M. Liberati, E. Arenholz, H. Ohldag and J. Stöhr, *Phys. Rev. Lett.*, 2004, **92**, 247201.
- 30 A. Fraile Rodríguez, A. C. Basaran, R. Morales, M. Kovylyna, J. Llobet, X. Borrísé, M. A. Marcus, A. Scholl, I. K. Schuller, X. Batlle and A. Labarta, *Phys. Rev. B*, 2015, **92**, 174417.
- 31 M. Kovylyna, R. Morales, A. Labarta and X. Batlle, *Phys. Rev. B*, 2012, **86**, 224414.
- 32 R. Morales, M. Vélez, O. Petravic, I. V. Roshchin, Z.-P. Li, X. Batlle, J. M. Alameda and I. K. Schuller, *Appl. Phys. Lett.*, 2009, **95**, 092503.
- 33 Z.-P. Li, O. Petravic, R. Morales, J. Olamit, X. Batlle, K. Liu and I. K. Schuller, *Phys. Rev. Lett.*, 2006, **96**, 217205.
- 34 O. Petravic, Z.-P. Li, I. V. Roshchin, M. Viret, R. Morales, X. Batlle and I. K. Schuller, *Appl. Phys. Lett.*, 2005, **87**, 222509.
- 35 M. R. Fitzsimmons, D. Lederman, M. Cheon, H. Shi, J. Olamit, I. V. Roshchin and I. K. Schuller, *Phys. Rev. B*, 2008, **77**, 224406.
- 36 A. C. Basaran, T. Saerbeck, J. de la Venta, H. Huckfeldt, A. Ehresmann and I. K. Schuller, *Appl. Phys. Lett.*, 2014, **105**, 072403.
- 37 P. Gaunt, *J. Appl. Physiol.*, 1986, **59**, 4129–4132.